Microwave Generation in Synchronized Semiconductor Superlattices

M. B. Gaifullin,[1] N. V. Alexeeva,[1,2] A. E. Hramov,[3,4] V. V. Makarov,[3] V. A. Maksimenko,[3] A. A. Koronovskii,[3,4] M. T. Greenaway,[1] T. M. Fromhold,[2] A. Patanè,[2] C. J. Mellor,[2] F. V. Kusmartsev,[1] and A. G. Balanov[1]

[1]*Department of Physics, Loughborough University, Loughborough LE11 3TU, United Kingdom*
[2]*School of Physics and Astronomy, University of Nottingham, Nottingham NG7 2RD, United Kingdom*
[3]*Yuri Gagarin State Technical University of Saratov, Politechnicheskaja 77, Saratov, 410054, Russia*
[4]*Faculty of Nonlinear Processes, Saratov State University, Astrakhanskaya 83, Saratov, 410012, Russia*

(Received 22 September 2016; revised manuscript received 13 February 2017; published 27 April 2017)

We study high-frequency generation in a system of electromagnetically coupled semiconductor superlattices fabricated on the same doped substrate. Applying a bias voltage to a single superlattice generates high-frequency current oscillations. We demonstrate that within a certain range of the applied voltage, the current oscillations within the superlattices can be self-synchronized, which leads to a dramatic rise in the generated microwave power. These results, which are in good agreement with our numerical model, open a promising practical route towards the design of high-power miniature microwave generators.

DOI: 10.1103/PhysRevApplied.7.044024

I. INTRODUCTION

Emergent phenomena resulting from the complex cooperative behavior of coupled elements are among the most topical and important subjects of modern physical science. These phenomena cannot be observed in individual elements and come into existence only due to an interaction between entities. Recent examples in condensed matter physics embrace such interesting findings as monopoles in spin ice [1], Skyrmion lattices in chiral magnets [2], and light-induced superconductivity [3,4]. Other instances of emergent behavior relate to dynamical self-organization such as dynamical phases of a driven Bose-Einstein condensate [5], synchronization of micromechanical oscillators coupled through an optical radiation field [6], and coherent terahertz emission from layered high-temperature superconductors [7,8].

Here we investigate cooperative effects in the generation of microwaves from an array of miniband semiconductor superlattices (SLs) [9,10] arranged on the same doped substrate. Once the bias voltage exceeds a certain threshold, each individual SL exhibits current oscillations produced by moving charge domains [11,12]. Our measurements for two nonidentical superlattices show that despite the frequencies of the single SLs being considerably different from each other, electromagnetic (EM) coupling mediated by the substrate can force all of the SLs to generate current oscillations at the same frequency, thus, producing frequency synchronization [13,14]. Moreover, within a certain range of the applied voltage, the synchronization phenomena can significantly (up to 300%) enhance the collective microwave power output. Our measurements are in a good agreement with the results of corresponding numerical simulations. Further numerical investigations show that synchronization is possible for three and four SLs on the same substrate, leading to an even more dramatic increase in the generated ac power. Earlier experimental work has demonstrated that charge domains traveling along miniband SLs are able to produce current oscillations with frequencies up to 300 GHz [15]. Thus, our results suggest a way to solve the long-standing problem of power amplification in solid-state generators operating in the subterahertz or terahertz regime.

II. EXPERIMENTAL RESULTS

In our experiments, we use three SLs grown on the same Si-doped 500-μm-thick GaAs substrate (Fig. 1). Each SL consists of 15 periods, which are separated from two heavily n-doped GaAs contacts by Si-doped GaAs layers of width 50 nm and doping concentration of 1×10^{17} cm^{-3}. Each SL period, which is Si doped at 3×10^{16} cm^{-3}, includes a 1-nm AlAs barrier, a 7-nm GaAs quantum well, and a 0.8 InAs monolayer at the center of each quantum well. The latter enhances electron injection from a doped contact layer into the first miniband and inhibits interminiband tunneling [16]. The SLs are processed into circular mesa structures with Ohmic contacts to the substrate

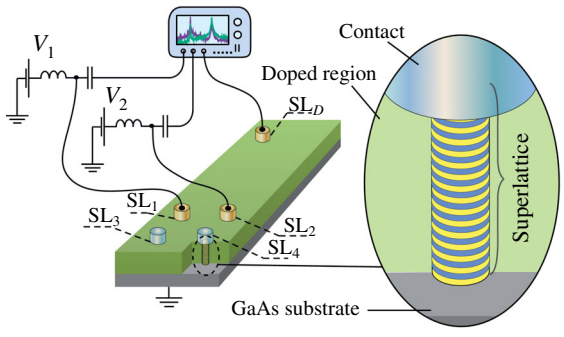

FIG. 1. The design of the experimental setup. Generators $SL_{1,2}$ and the detector SL_D (gold) are involved in our experiments. $SL_{3,4}$ (blue) are additional devices used in our numerical simulations.

and top cap layer. A sketch of the sample is shown in Fig. 1. In our study, we measure the microwave generation from the SLs labeled SL_1 and SL_2 in Fig. 1, which are separated by 100 μm. Each device has the same mesa diameter of 20 μm and an independent power supply, as shown in Fig. 1. A LeCroy SDA 18000 serial data analyzer is used to measure the spectra of oscillations generated by the SLs. All measurements are performed at room temperature.

First, we consider how the EM output of each SL depends on the bias voltage when the second SL is not powered. Our measurements show that each SL is able to generate microwave current oscillations for an applied voltage V in the range 0.26–0.35 V. Figures 2(a) and 2(b) illustrate the fundamental frequency f [Fig. 2(a)] and the power P [Fig. 2(b)] of the microwave signal generated by SL_1 (purple curve) and SL_2 (green curve) as a function of $V_{1,2}$. Although the SLs demonstrate very similar $P(V_{1,2})$ dependences [Fig. 2(b)] and I-V curves [inset in Fig. 2(b)], the frequencies f of the signals measured from different devices are significantly different at all values of the voltage applied. As Fig. 2(a) reveals, SL_1 generates signals in the frequency range 562–621 MHz, while SL_2 has a generation range 690–722 MHz. This difference in the generated frequencies can originate from variation of the contacts and leads attached to a particular SL and corresponding differences in the parasitic capacitance and inductances of the SL circuits [17,18].

Next, we investigate how the microwave output of each SL is affected by simultaneous generation from another SL. To do this, we fix the voltage V_2 applied to SL_2 at 295 mV and measure the spectra of the voltage oscillations on the contacts of both SLs for different voltages V_1 applied to SL_1. Figure 3(a) illustrates the effect of changing V_1 on the fundamental frequencies f corresponding to the dominant spectral peaks of the two SLs. For small $V_1 = 260$ mV (dashed line 1 in Fig. 3), the power of the harmonic at the fundamental frequency of SL_2 significantly exceeds that of SL_1. Therefore, the frequency of the dominant peak in the spectrum of SL_1 coincides with the fundamental frequency of SL_2. This is also confirmed by Fig. 4(a), which shows that the spectral peak induced by the contribution from SL_2

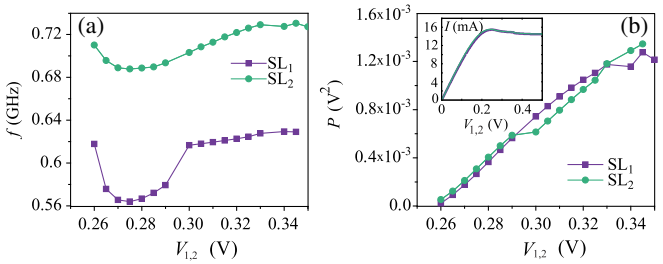

FIG. 2. (a) Fundamental frequencies measured for the single SLs and (b) power of the generated signals measured for different bias voltages. The purple squares correspond to the data measured from SL_1 and green circles refer to SL_2. The inset in (b) shows the I-V characteristic of SL_1 (purple) and SL_2 (green).

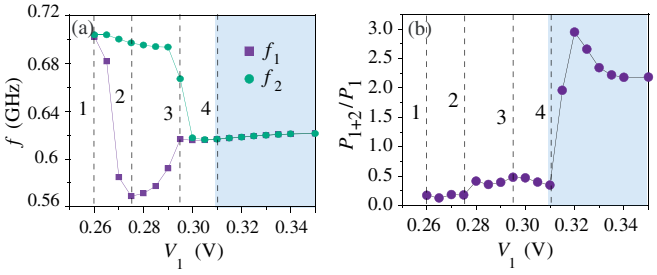

FIG. 3. Experimental dependence of (a) the SL fundamental frequencies on V_1 and (b) the relative power of the signal measured from SL_D versus V_1 for $V_2 = 295$ mV. In (a) the purple squares correspond to the data measured from SL_1 and green circles refer to SL_2. The synchronization region is highlighted in gray. The vertical dashed lines with numbers correspond to the values of V_1 discussed in the text.

(around 700 MHz) is much higher than that corresponding to the generation from SL_1 (around 600 MHz). With increasing V_1 (dashed line 2 in Fig. 3), the dominant peaks first diverge [Fig. 4(b)], but for $V_1 > 275$ mV (dashed line 3 in Fig. 3), they start to converge [Fig. 4(c)], and at $V_1 \approx 305$ mV (dashed line 4 in Fig. 3), they coincide [Fig. 4(d)]. For higher V_1, the peak frequencies are locked, manifesting the onset of synchronization [14].

In order to study the collective high-frequency output from SL_1 and SL_2, we use an unpowered element SL_D as a detector (Fig. 1), which is placed 400 μm away from SL_1. The detector has a mesa diameter of 5 μm and an almost linear I-V curve for bias voltages in the range -300 to $+300$ mV. The relative power of the voltage oscillations measured from SL_D for different V_1 is displayed in Fig. 3(b). This characteristic is the ratio between the total ac power P_{1+2} measured from SL_D, when both SL_1 and SL_2 are generating microwaves ($V_2 = 295$ mV) and the power P_1 measured when only SL_1 is active

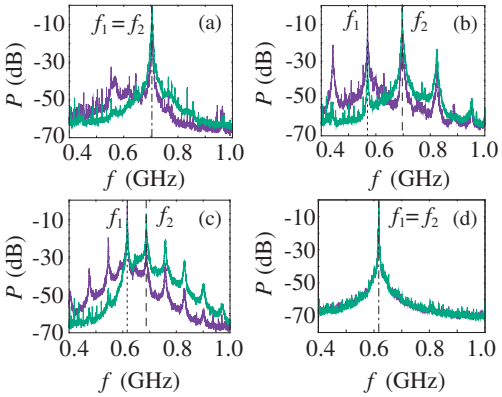

FIG. 4. Power spectra of the voltage oscillations in SL_1 (purple) and SL_2 (green) measured for the various values of V_1: 260 (a), 275 (b), 295 (c), and 310 mV (d) indicated in Fig. 3 by the dashed lines 1,2,3,4, respectively. Positions of the fundamental frequencies are marked in the spectra by dotted (SL_1) and dashed (SL_2) lines.

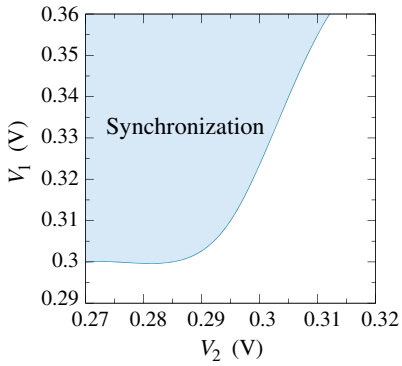

FIG. 5. Experimental region of synchronization (shaded) in the (V_2, V_1) parameter plane.

$(V_2 = 0)$. A comparison of Figs. 3(a) and 3(b) reveals that in the absence of synchronization, the microwave power collected from SL_D is less than that in the case of a single generating element. However, under certain conditions, the frequency locking can yield a significant boost (up to 3 times) of the detected microwave power. We find that the synchronization phenomena associated with frequency locking can be achieved for a range of the voltages V_1 and V_2, as shown by the shaded area in Fig. 5. Thus, the experiment shows that a stable synchronization regime is possible even for SLs with a large initial frequency mismatch.

III. THEORETICAL MODELING

To gain deeper insight into the results of the experiments, we theoretically model the system under study. For this aim, we describe the charge transport in each SL using a self-consistent system of Poisson and continuity equations, as discussed in Refs. [12,18]. Within this approach, the SL is split into layers [see Fig. 6(a)], and the discretized forms of the transport equations are solved numerically. Thus, the time evolution of charge density $n_m(t)$ in the mth layer is determined by the equation

$$e\Delta x \frac{dn_m}{dt} = J_{m-1} - J_m, \qquad m = 1, \ldots, N, \tag{1}$$

where e is the electron charge, and J_{m-1}, J_m are the volume current densities on the left and right boundaries of the mth layer. The latter can be calculated as

$$J_m = e n_m v_d(\bar{F}_m), \tag{2}$$

where $\bar{F}_m$ is the mean field in the mth layer [11,12]. It is assumed that charge transport is realized within the lowest miniband when interminiband tunneling can be neglected. In this case, the miniband drift velocity v_d for the finite temperature T and given $\bar{F}_m$ can be calculated using the Esaki-Tsu-Romanov formalism [19]:

$$v_d(\bar{F}) = \frac{\Delta d}{2\hbar} \frac{I_1(\Delta/2k_BT)}{I_0(\Delta/2k_BT)} \frac{e\bar{F}d\tau/\hbar}{1 + (e\bar{F}d\tau/\hbar)^2}, \tag{3}$$

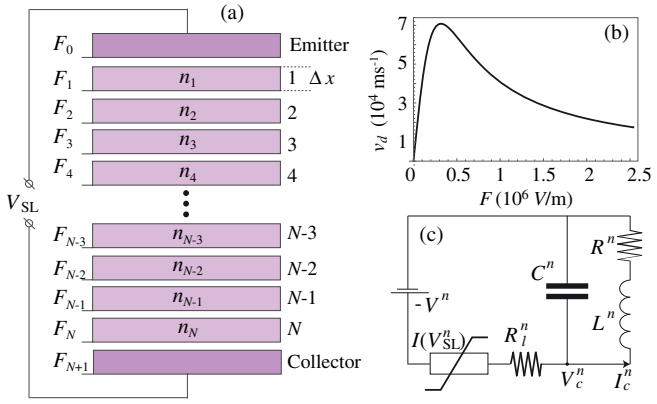

FIG. 6. (a) Schematic representation of the numerical model describing the charge transport in the SL. (b) $v_d(F)$ calculated for electrons in the first miniband of the superlattice under study. (c) Equivalent circuit of SL_n $(n = 1, 2, D)$, where C^n, L^n, and R^n are the equivalent capacitance, inductance, and resistance, $I(V^n_{SL})$ is the current through the SL, with voltage V^n_{SL} dropped across it, and V_n is the dc supply voltage. The load resistance is $R^n_l = 0.1\ \Omega$.

where $d = 8.3$ nm is the period of the SL, $\Delta = 19.1$ meV is the miniband width, and τ is an effective scattering time, which takes into account both elastic and inelastic scattering events [11,20]. Parameter k_B represents the Boltzmann constant, and $I_n(x)$, where $n = 0$, 1, is a modified Bessel function of the first kind. In our calculations, we fix $T = 4.2$ K and $\tau = 176$ fs, whose value corresponds to recent experiments [17,18,20]. The dependence of electron drift velocity v_d on electric field strength F is shown in Fig. 6(b). The function $v_d(F)$ has a characteristic maximum, which is associated with onset of Bloch oscillations. For large F, the effect of Bloch oscillations on electron dynamics becomes stronger. This leads to increased localization of the electron orbits and decrease of v_d. Although Eq. (3) is obtained for a static electric field F, it can also be used for a slowly oscillating electric field, when the miniband electrons can follow the ac field adiabatically [21–23], i.e., for $2\pi f\tau \ll 1$, where f is the frequency of an applied electric field. We note that for the value of τ used in our model, this adiabatic limit spans up to several hundred gigahertz.

The electric field F_m at the left-hand edge of the mth layer [Fig. 6(a)] is determined by the discretized Poisson equation

$$F_{m+1} = \frac{e\Delta x}{\varepsilon_0\varepsilon_r}(n_m - n_D) + F_m, \qquad m = 1, \ldots, N. \tag{4}$$

Here, ε_0 and $\varepsilon_r = 12.5$ are the absolute and relative permittivities, respectively, and $n_D = 3 \times 10^{22}$ m^{-3} is the n-type doping density in the SL layers [20]. To ensure convergence of the numerical solutions, we set $N = 480$ and $\Delta x = 0.24$ nm [12,18].

Ohmic boundary conditions determine the current $J_0 = \sigma F_0$ in the heavily doped emitter of electrical conductivity $\sigma = 3788$ Sm^{-1} [20]. The voltage V^n_{SL} applied to the nth SL is a global constraint given by

$$V_{\mathrm{SL}}^{n} = U + \frac{\Delta x}{2}\sum_{m=1}^{N}(F_m + F_{m+1}), \tag{5}$$

where the voltage U dropped across the contacts includes the effect of charge accumulation and depletion in the emitter and collector regions and the contact resistance $R = 17\ \Omega$ [24,25]. We calculate the current through the SL as

$$I^{n}(t) = \frac{A}{N+1}\sum_{m=0}^{N} J_m, \tag{6}$$

where $A = 5\times10^{-10}\ \mathrm{m}^2$ is the cross-sectional area of the SL [11,12,20]. To take into account the impedance imposed by the contacts and the leads, we model each SL connected to an equivalent LRC (resonant) circuit [17,18,26]; see Fig. 6(c).

The current $I(t)$ generated by each SL depends on the voltage V_{SL}^{n} applied to this device, where $n = 1, 2$, and D is the index of the given SL. This voltage includes a dc bias V_n and the ac voltage V_c^n induced by the LRC circuit, which, according to Fig. 6(c), can be described by the following equations:

$$C^{n}\frac{dV_c^{n}}{dt} = I(V_{\mathrm{SL}}^{n}) - I_c^{n}, \tag{7}$$

$$L^{n}\frac{dI_c^{n}}{dt} = -R^{n}I_c^{n} + V_c^{n} + R_l^{n}I(V_{\mathrm{SL}}). \tag{8}$$

Here, C^n, L^n, and R^n are the equivalent capacitance, inductance, and resistance of the circuit, respectively; R_l^n is the load resistance. The circuit parameters corresponding to our present experiment are summarized in Table I.

The dynamics of the EM field in the common substrate, which provides the coupling between SLs, is considered within the theory of microwave resonator excitation [27,28]. It is assumed that the substrate together with all leads, waveguides, and the measurement system form a single-mode resonator system, where the sth eigenmode $\mathbf{E}_s$ is excited. In this case, the longitudinal component of the electric field $E(\mathbf{r}, t)$ can be represented in the form $E = \mathrm{Re}[C_s(t)E_s(\mathbf{r})e^{j\omega_s t}]$, where E_s and ω_s are the spatial field distribution and frequency of the sth eigenmode of the resonator, and $C_s(t) = A(t)e^{j\psi(t)}$ is slowly varying compared to ω_s. The distance between the interacting SLs is less than several hundred micrometers, and the wavelength of the generated microwaves is around a few centimeters; therefore, we assume that the field distribution $E_s(\mathbf{r})$ in the region of the interacting SLs is homogeneous, and the electric field E in this region depends only on time t. According to the resonator excitation theory, the nonstationary equations for the slowly varying amplitude A and phase ψ are given by

$$\frac{dA}{dt} + \frac{\omega_s A}{2Q} = -\frac{\omega_s K}{2\pi L^2}\sum_{n=1}^{M} V_{\mathrm{SL}}^{n}\int_0^{2\pi} I^{n}(t)\cos(\omega_s t + \psi)d\omega_s t, \tag{9}$$

$$\frac{d\psi}{dt} = -\frac{\omega_s K}{2\pi L^2}\sum_{n=1}^{M} V_{\mathrm{SL}}^{n}\int_0^{2\pi} I^{n}(t)\sin(\omega_s t + \psi)d\omega_s t, \tag{10}$$

where L is the length of each SL, including the contact regions, K is the impedance of the resonator, Q is the quality factor for the sth resonator eigenmode, M is the number of SLs ($M = 3$ in our experiments), and $I^n(t)$ is the current through the nth SL [see Eq. (6)]. The parameters of the resonator system are estimated from the analysis of the experimental data: $f_s = \omega_s/2\pi = 0.6\,\mathrm{GHz}$, $Q = 2$, and $K = 400\ \Omega$. The voltage applied to the nth SL [see Eq. (5)] is defined through the equation $V_{\mathrm{SL}}^{n} = V_n - V_c^n + EL$, where V_n ($n = 1, 2$) is the bias voltage applied to the SL, and V_c^n is the voltage across the corresponding parasitic circuit [defined by Eqs. (7) and (8)]. Thus, the coupling between SLs is realized through the field E, while the electromagnetic properties of the substrate are taken into account via the parameters of the resonator.

We use the above model for numerical calculations of the device characteristics that are measured in experiment. Figure 7 shows the f values (a) and the relative power (b) of the voltage oscillations between the contacts of SL_D calculated as functions of V_1 for fixed $V_2 = 295$ mV. One can see that the plots in Fig. 7 are in good agreement with the measured data presented in Fig. 3. In both cases, the fundamental frequencies exhibit a similar dependence on V_1. Also, synchronization associated with the frequency

TABLE I. Circuit parameters for different SLs involved in calculations.

Superlattice	R_l^n	R^n	C^n	L^n
SL_1 ($n = 1$)	0.1 Ω	0.5 Ω	1.0 pF	0.05 nH
SL_2 ($n = 2$)	0.1 Ω	1.5 Ω	1.23 pF	0.07 nH
SL_D (detector SL)	0.1 Ω	0.5 Ω	1.0 pF	0.05 nH

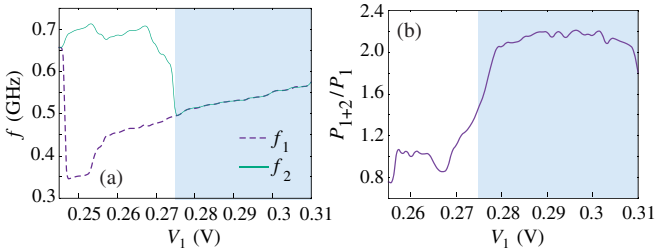

FIG. 7. Numerically calculated dependence of (a) the SL fundamental frequencies on the bias voltage V_{5M} and (b) the relative power of the signal at SL_D calculated versus V_1 when $V_2 = 295$ mV. The synchronization region is shaded. Corresponding experimental data are shown in Fig. 3.

locking leads to a dramatic increase in the power of the signal measured from SL_D. The difference between theory and experiment [cf. Figs. 3(b) and 7(b)], especially near the boundary of synchronization, can be explained by the simplifications made in our theoretical model. In particular, the assumption that the contact parameters are independent of the frequency and amplitude of V_n^{SL} can lead to inaccurate treatment of the reactance in the coupling of the SLs, which affects their collective dynamics. However, despite these simplifications, the numerically calculated region of synchronization shown in Figs. 7 and 8(a) resembles closely the experimental results in Figs. 3 and 5, respectively.

In Fig. 8, the color map represents the ac power P_{1+2} of the voltage oscillations in SL_D normalized to the maximal power $P_1 = 1.5\ \mu V^2$ of these oscillations in the case when only SL_1 generates microwaves ($V_2 = 0$). Figure 8(a) reveals that synchronization generally provides a significant increase in power [bright area in Fig. 8(a)]. However, in certain areas (marked orange or red) of the synchronization region (bounded by white dashed line), the power collected from SL_D is unaffected, or even weakened, by the frequency-locking phenomenon. We find that this depends on the phase difference $\Delta\phi$ between the locked signals. A color map representing the $\Delta\phi(V_2, V_1)$ variation is shown in Fig. 8(b). If the voltage oscillations on the contacts of SL_1 and SL_2 are in phase, $\Delta\varphi \approx 0$, they may constructively interfere, thereby increasing the power measured at SL_D [compare Figs. 8(a) and 8(b)]. By contrast, antiphase synchronization $\Delta\varphi \approx \pm\pi$ will produce destructive interference of the generated signals and, thus, suppress the output from the detector. In the absence of synchronization, the phase difference changes with time, preventing the coherent summation of the output from the generating SLs. We note that the relative power in Figs. 3(b) and 7(b) does not achieve the theoretical maximum value $M^2 = 4$ (here, M is a number of the generating SLs), which is expected when two identical signals being in phase are summed up in the same detector. This discrepancy occurs because the SLs involved in the interaction are not identical and, as we mention above, initially have a significant frequency

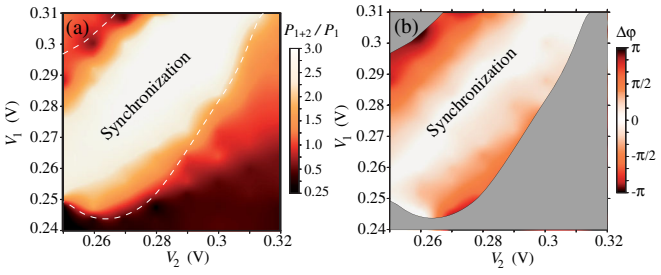

FIG. 8. (a) The dependence $P_{1+2}(V_2, V_1)/P_1$ obtained in numerical simulation. The white dashed line bounds the synchronization region; (b) $\Delta\varphi$ within the synchronization region, gray area corresponds to the absence of synchronization.

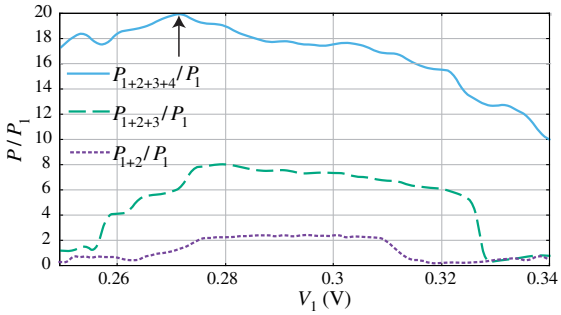

FIG. 9. Numerically calculated relative power collected from SL_D versus V_1 for two (dotted), three (dashed), and four (solid) interacting SLs. The voltage applied to all SLs, except SL_1, is 295 mV.

mismatch. The latter prevents the generation of the identical current oscillations, even in the case of synchronization.

Finally, we check whether synchronization can be achieved for a larger number of interacting SLs located on the same substrate. In our numerical calculations, we assume that all additional SLs have parameters identical to SL_2 (see Table I). If the in-phase synchronization is achieved, we expect that the superposition of M-synchronized signals will produce an M^2 up scaling of the relative power. Our simulations predict that (i) synchronization of SLs coupled through the substrate is possible even for a larger number of elements, and (ii) synchronization can dramatically increase the ac power collected from the detector. The result of our calculations is presented in Fig. 9, where the dependences of the relative power P detected by SL_D are shown versus V_1 for two (dotted curve), three (dashed curve), and four (solid curve) SLs ($V_{2,3,4} = 295$ mV). As expected, the figure reveals that the increase of output power is associated with the onset of synchronization, and the maximal power is realized when the phase difference between signals generated from different SLs is close to zero. For $M = 3$, the relative power P_{1+2+3}/P_1 achieves a value of approximately 8, which is close to, but still less than, M^2. As before, such disagreement is caused by differences between SL_1 and the other SLs that are coupled to it. It is surprising, therefore, that when $M = 4$, we observe a 20-fold increase of the output power, which considerably exceeds $M^2 = 16$. We find that this is because the voltage induced at the contacts of SL_D exceeds the threshold value, and so SL_D starts to generate high-frequency power on its own. In addition, the total power pumped into the resonator becomes large enough for it to demonstrate a visible resonant response.

IV. CONCLUSION

In conclusion, we show both theoretically and in experiment that EM generation from SLs fabricated on the same substrate can be synchronized due to EM interaction through the substrate. Remarkably, the synchronization is possible even if the individual SLs have a large

fundamental frequency mismatch and can lead to dramatic increase of output power, e.g., up to 3 times for two SLs, and up to 20 times for four SLs. Thus, our results provide an efficient way to create powerful solid-state generators able to work at room temperature and at very high frequency (potentially up to the terahertz range). Our calculations also show that the electrodynamics of the substrate play an important role in coupling the SLs and in realizing synchronization with a particular phase difference. These findings opens a path to developing a type of active device comprising an array of generating nanostructures, which are fabricated on an appropriately shaped coupling substrate [29,30]. Moreover, synchronization mediated by the substrate has the potential to boost the power generated from other superlattice-based devices, e.g., quantum cascade lasers [31], arrays of Josephson junctions [32–34], or van der Waals heterostructures [35,36].

ACKNOWLEDGMENTS

This work is supported by the Engineering and Physical Sciences Research Council (Grants No. EP/K503800/1 and No. EP/M016099/1). The numerical studies of the synchronization of the semiconductor superlattices is supported by the Russian Foundation for Basic Research (Grants No. 15-02-00624-a and No. 16-32-00272-mol-a). A. E. H. also acknowledges support from the Ministry of Education and Science of Russian Federation (Project No. 3.4593.2017/VU). We are grateful to K. Alekseev for helpful discussions and M. Henini for growing the samples.

[1] C. Castelnovo, R. Moessner, and S. L. Sondhi, Magnetic monopoles in spin ice, Nature (London) **451**, 42 (2008).

[2] S. Mühlbauer, B. Binz, F. Jonietz, C. Pfleiderer, A. Rosch, A. Neubauer, R. Georgii, and P. Böni, Skyrmion lattice in a chiral magnet, Science **323**, 915 (2009).

[3] M. Mitrano, A. Cantaluppi, D. Nicoletti, S. Kaiser, A. Perucchi, S. Lupi, P. Di Pietro, D. Pontiroli, M. Riccò, S. R. Clark, D. Jaksch, and A. Cavalleri, Possible light-induced superconductivity in K3C60 at high temperature, Nature (London) **530**, 461 (2016).

[4] J. Demsar, Light-induced superconductivity, Nat. Phys. **12**, 202 (2016).

[5] F. Piazza and H. Ritsch, Self-Ordered Limit Cycles, Chaos, and Phase Slippage with a Superfluid inside an Optical Resonator, Phys. Rev. Lett. **115**, 163601 (2015).

[6] M. Zhang, S. Shah, J. Cardenas, and M. Lipson, Synchronization and Phase Noise Reduction in Micromechanical Oscillator Arrays Coupled through Light, Phys. Rev. Lett. **115**, 163902 (2015).

[7] L. Ozyuzer, A. E. Koshelev, C. Kurter, N. Gopalsami, Q. Li, M. Tachiki, K. Kadowaki, T. Yamamoto, H. Minami, H. Yamaguchi, T. Tachiki, K. E. Gray, W.-K. Kwok, and U. Welp, Emission of coherent THz radiation from superconductors, Science **318**, 1291 (2007).

[8] U. Welp, K. Kadowaki, and R. Kleiner, Superconducting emitters of THz radiation, Nat. Photonics **7**, 702 (2013).

[9] L. Esaki and R. Tsu, Superlattice and negative differential conductivity in semiconductors, IBM J. Res. Dev. **14**, 61 (1970).

[10] A. A. Ignatov and Yu. A. Romanov, Nonlinear electromagnetic properties of semiconductors with a superlattice, Phys. Status Solidi B **73**, 327 (1976).

[11] A. Wacker, Semiconductor superlattices: A model system for nonlinear transport, Phys. Rep. **357**, 1 (2002).

[12] M. T. Greenaway, A. G. Balanov, E. Schöll, and T. M. Fromhold, Controlling and enhancing terahertz collective electron dynamics in superlattices by chaos-assisted miniband transport, Phys. Rev. B **80**, 205318 (2009).

[13] A. S. Pikovsky, M. G. Rosenblum, and J. Kurths, *Synchronization: A Universal Concept in Nonlinear Sciences* (Cambridge University Press, Cambridge, England, 2001).

[14] A. G. Balanov, N. B. Janson, D. E. Postnov, and O. V. Sosnovtseva, *Synchronization: From Simple to Complex* (Springer, New York, 2009).

[15] H. Eisele, S. P. Khanna, and E. H. Linfield, Superlattice electronic devices as high-performance oscillators between 60–220 GHz, Appl. Phys. Lett. **96**, 072101 (2010).

[16] A. Patanè, D. Sherwood, L. Eaves, T. M. Fromhold, M. Henini, P. C. Main, and G. Hill, Tailoring the electronic properties of GaAs/AlAs superlattices by InAs layer insertions, Appl. Phys. Lett. **81**, 661 (2002).

[17] N. Alexeeva, M. T. Greenaway, A. G. Balanov, O. Makarovsky, A. Patanè, M. B. Gaifullin, F. Kusmartsev, and T. M. Fromhold, Controlling High-Frequency Collective Electron Dynamics via Single-Particle Complexity, Phys. Rev. Lett. **109**, 024102 (2012).

[18] A. E. Hramov, V. V. Makarov, A. A. Koronovskii, S. A. Kurkin, M. B. Gaifullin, N. V. Alexeeva, K. N. Alekseev, M. T. Greenaway, T. M. Fromhold, A. Patanè, F. V. Kusmartsev, V. A. Maksimenko, O. I. Moskalenko, and A. G. Balanov, Subterahertz Chaos Generation by Coupling a Superlattice to a Linear Resonator, Phys. Rev. Lett. **112**, 116603 (2014).

[19] Yu. A. Romanov, Nonlinear effects in periodic semiconductor structures, Opt. Spectrosc. **33**, 917 (1972).

[20] T. M. Fromhold, A. Patane, S. Bujkiewicz, P. B. Wilkinson, D. Fowler, D. Sherwood, S. P. Stapleton, A. A. Krokhin, L. Eaves, M. Henini, N. S. Sankeshwar, and F. W. Sheard, Chaotic electron diffusion through stochastic webs enhances current flow in superlattices, Nature (London) **428**, 726 (2004).

[21] E. Schomburg, A. A. Ignatov, J. Grenzer, K. F. Renk, D. G. Pavel'ev, Yu. Koschurinov, B. Ja. Melzer, S. Ivanov, S. Schaposchnikov, and P. S. Kop'ev, Suppression of current through an Esaki-Tsu GaAs/AlAs superlattice by millimeter wave irradiation, Appl. Phys. Lett. **68**, 1096 (1996).

[22] S. Winnerl, E. Schomburg, J. Grenzer, H.-J. Regl, A. A. Ignatov, A. D. Semenov, K. F. Renk, D. G. Pavel'ev, Yu. Koschurinov, B. Melzer, V. Ustinov, S. Ivanov, S. Schaposchnikov, and P. S. Kop'ev, Quasistatic and dynamic interaction of high-frequency fields with miniband electrons in semiconductor superlattices, Phys. Rev. B **56**, 10303 (1997).

[23] F. Klappenberger, K. N. Alekseev, K. F. Renk, R. Scheuerer, E. Schomburg, S. J. Allen, G. R. Ramian, J. S. S. Scott, A. Kovsh, V. Ustinov, and A. Zhukov, Ultrafast creation and annihilation of space-charge domains in a semiconductor superlattice observed by use of terahertz fields, Eur. Phys. J. B **39**, 483 (2004).

[24] M. T. Greenaway, A. G. Balanov, and T. M. Fromhold, in *Nonlinear Laser Dynamics. From Quantum Dots to Cryptography*, edited by K. Lüdge (Wiley-VCH Verlag & Co. KGaA, Weinheim, 2012), p. 111.

[25] A. G. Balanov, M. T. Greenaway, A. A. Koronovskii, O. I. Moskalenko, A. O. Sel'skii, T. M. Fromhold, and A. E. Hramov, The effect of temperature on the nonlinear dynamics of charge in a semiconductor superlattice in the presence of a magnetic field, J. Exp. Theor. Phys. **114**, 836 (2012).

[26] V. V. Makarov, A. E. Hramov, A. A. Koronovskii, K. N. Alekseev, V. A. Maksimenko, M. T. Greenaway, T. M. Fromhold, O. I. Moskalenko, and A. G. Balanov, Subterahertz amplification in a semiconductor superlattice with moving charge domains, Appl. Phys. Lett. **106**, 043503 (2015).

[27] R. E. Collin, *Foundations for Microwave Engineering*, 2nd ed., IEEE Press Series on Electromagnetic Wave Theory (John Wiley and Sons, Inc., Hoboken, NJ, 2001).

[28] L. A. Vainshtein, *Electromagnetic Waves* (Izdatel'stvo Radio i Sviaz', Moscow, 1988).

[29] H.-T. Chen, W. J. Padilla, J. M. O. Zide, A. C. Gossard, A. J. Taylor, and R. D. Averitt, Active terahertz metamaterial devices, Nature (London) **444**, 597 (2006).

[30] S. Suzuki, M. Shiraishi, H. Shibayama, and M. Asada, High-power operation of terahertz oscillators with resonant tunneling diodes using impedance-matched antennas and array configuration, IEEE J. Sel. Top. Quantum Electron. **19**, 8500108 (2013).

[31] R. Köhler, A. Tredicucci, F. Beltran, H. E. Beere, E. H. Linfield, A. G. Davies, D. A. Ritchie, R. Iotti, and F. Rossi, Terahertz semiconductor-heterostructure laser, Nature (London) **417**, 156 (2002).

[32] L. Ozyuzer, A. E. Koshelev, C. Kurter, N. Gopalsami, Q. Li, M. Tachiki, K. Kadowaki, T. Yamamoto, H. Minami, H. Yamaguchi, T. Tachiki, K. E. Gray, W.-K. Kwok, and U. Welp, Emission of coherent THz radiation from superconductors, Science **318**, 1291 (2007).

[33] M. Tachiki, M. Iizuka, K. Minami, S. Tejima, and H. Nakamura, Emission of continuous coherent terahertz waves with tunable frequency by intrinsic Josephson junctions, Phys. Rev. B **71**, 134515 (2005).

[34] F. Song, F. Müller, R. Behr, and A. M. Klushin, Coherent emission from large arrays of discrete Josephson junctions, Appl. Phys. Lett. **95**, 172501 (2009).

[35] A. Mishchenko *et al.*, Twist-controlled resonant tunnelling in graphene/boron nitride/graphene heterostructures, Nat. Nanotechnol. **9**, 808 (2014).

[36] J. Gaskell, L. Eaves, K. S. Novoselov, A. Mishchenko, A. K. Geim, T. M. Fromhold, and M. T. Greenaway, Graphene-hexagonal boron nitride resonant tunneling diodes as high-frequency oscillators, Appl. Phys. Lett. **107**, 103105 (2015).